International Journal of Thermal Sciences 221 (2026) 110501

Contents lists available at ScienceDirect

International Journal of Thermal Sciences

journal homepage: www.elsevier.com/locate/ijts

Enhanced heat conduction in diamond/copper composites via interconnected structures: Machine learning molecular dynamics simulation ☆

Bin Liu [a], Zhiguo Tian [a], Alexander A. Barinov [b], Moran Wang [a,*]

[a] Key Laboratory for Thermal Science and Power Engineering of Ministry of Education, Department of Engineering Mechanics, Tsinghua University, Beijing 100084, China

[b] Department of Thermophysics, Bauman Moscow State Technical University, Moscow 105005, Russia

ARTICLE INFO

Dataset link: https://github.com/binliu93/Data_for_diamond-Cu

Keywords:
Diamond/copper composite
Interconnected network structure
Machine learning potential
Molecular dynamics simulation
Phonon thermal transport

ABSTRACT

Diamond/Cu composites have attracted considerable attention for thermal management applications due to their outstanding thermal conductivity. Recent studies have demonstrated that interconnected diamond network structures can significantly enhance the heat conduction of diamond/Cu composites, while the underlying microscopic heat transfer mechanisms remain to be fully elucidated. This study employed machine learning molecular dynamics simulations to validate and elucidate the heat conduction enhancement mechanisms of interconnected network structures. We developed a machine learning potential for diamond/Cu heterostructures based on the neuroevolution potential model and calculated the lattice thermal conductivity (LTC) of two series of network structures: diamond network/Cu (DN/Cu) and Cu network/diamond (CuN/D). The results demonstrate that DN/Cu exhibits monotonically increasing LTC with diamond content due to continuous heat transfer channels, while CuN/D shows non-monotonic behavior with a minimum LTC at intermediate diamond fractions, originating from the competitive mechanism between contributions from low-frequency Cu phonons (0–8 THz) and high-frequency diamond phonons (10–40 THz) to thermal transport. Through spectral LTC decomposition and wavelike phonon transmission analysis, we elucidated the suppressive effects of multiple heat transfer mechanisms on LTC, including phonon interfacial scattering, coherent interference effects, and total internal reflection in nano-network structures. This work establishes quantitative design thresholds for lattice thermal transport in DN/Cu, revealing a critical diamond volume fraction of ~30% above which DN/Cu consistently outperforms CuN/D, and an unexpected LTC minimum at ~50% diamond in CuN/D structures driven by phonon frequency competition. These findings explain why diamond network structures, despite demonstrating significant heat conduction enhancement compared to dispersed particles, still exhibit LTC values substantially lower than pure diamond, thus revealing substantial room for design optimization of network architectures.

1. Introduction

Heat spreading is a critical aspect of electronic thermal management that effectively reduces thermal gradients and prevents hotspot formation. With the continuous increase in power density of electronic devices, conventional heat spreaders such as metals and ceramics are gradually unable to meet practical requirements due to their inherent thermal conductivity limitations. Diamond/metal composites (DMCs) based heat spreaders have recently garnered extensive attention due to their excellent thermal conductivity, mechanical properties, and tunability of thermal expansion coefficient [1,2]. As a representative example of DMCs, diamond/Cu composites integrate the high thermal conductivity of diamond with the excellent processability and mechanical properties of Cu, demonstrating outstanding thermal management potential [3]. To further enhance the thermal conductivity of diamond/Cu composites, strategies such as increasing the concentration, distribution uniformity, and size of diamond particles can be employed [4–6]. However, due to significant differences between diamond and Cu in crystal structure, chemical properties, and thermal expansion coefficients, interfacial mismatch and thermal resistance become critical bottlenecks constraining the overall heat conduction enhancement of their composites. To address this issue, research has

☆ This article is part of a Special issue entitled: 'Micro/Nanoscale Transport' published in International Journal of Thermal Sciences.

* Corresponding author.
E-mail address: mrwang@tsinghua.edu.cn (M. Wang).

https://doi.org/10.1016/j.ijthermalsci.2025.110501
Received 26 August 2025; Received in revised form 18 November 2025; Accepted 18 November 2025
Available online 25 November 2025

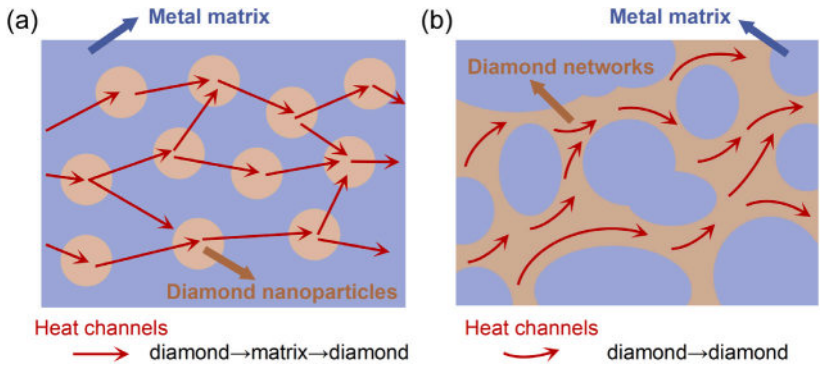

Fig. 1. Schematic illustration of heat channels in DMCs with (a) dispersed diamond particles and (b) interconnected diamond networks [17].

primarily focused on reducing phonon scattering through various interfacial engineering approaches, including interlayer design [7–9], surface modification [6,10,11], and interfacial alloying [12,13].

Recent research has transitioned from traditional DMCs with metal matrix/diamond particle reinforcement toward innovative structural designs that allow further enhancement of heat conduction [1]. Gradient multilayer design can significantly improve heat conduction in diamond/Cu composites. For example, high thermal conductivity of 549 $W \cdot m^{-1} \cdot K^{-1}$ can be achieved through diamond/graphite/TiC/Cr_3C_2/Cu gradient structures [14]. Structure-function integrated design achieves synergistic enhancement of heat dissipation structures and heat conduction by combining geometric optimization with functional design. This includes integrated design of diamond microchannels with microporous Cu, utilizing excellent thermal diffusion along triangular channels and optimized heat transfer to boiling fluids [15], as well as novel fin geometries with hyperbolic, wavy, and corrugated configurations, where diamond/Cu composites achieve 95% performance improvement on hyperbolic fin surfaces compared to traditional designs [16].

Most notably, the recent proposal of interconnected network structures represents a paradigm shift by replacing dispersed diamond particles with interconnected structures, creating effective heat transfer channels and significantly reducing the impact of interfacial thermal resistance (Fig. 1). This approach enables rapid thermal response and promotes efficient heat transfer throughout the composite material, ultimately achieving an impressive thermal conductivity of 315 $W \cdot m^{-1} \cdot K^{-1}$ with only 4.6 vol% diamond content [17]. The thermal conductivity values mentioned above represent the total thermal conductivity, which includes contributions from both phonons and electrons.

These innovative structural designs offer several advantages over traditional DMCs. Structural optimization enables enhanced thermal performance without simply increasing diamond content, thereby reducing material costs and processing complexity. Functional integration allows these designs to simultaneously address multiple thermal management requirements, such as heat spreading, thermal interface optimization, and temperature uniformity. Design flexibility provides opportunities to tailor thermal properties for specific applications through controlled microstructure engineering. However, these advanced designs also present notable challenges. The high degree of design freedom in structural parameters makes systematic performance optimization difficult, as the interplay between geometric variables, material properties, and processing conditions creates complex multidimensional design spaces. Moreover, the intricate heat transport mechanisms within these complex structures involve multiscale physics phenomena [18–25], including phonon transport across interfaces, multiple scattering of phonons in heterogeneous networks, and coupled heat transfer modes that are not fully understood. This complexity necessitates the development of comprehensive theoretical models and computational tools to predict thermal behavior, guide design optimization, and accelerate the development of next-generation thermal management solutions.

Molecular dynamics (MD) simulation plays an important role in understanding and designing thermal transport properties of complex materials [18]. Compared to methods such as phonon Green's function and Boltzmann transport equation [21,26–29], MD can capture phonon–phonon scattering of arbitrary order and naturally capture phonon scattering caused by other sources such as defects and mass disorder. The predictive capability of MD simulations is highly dependent on the accuracy of interatomic potentials. In recent years, machine learning potentials (MLPs) have demonstrated significant potential in achieving the requisite accuracy for diverse material systems [30–33]. MLPs capture interatomic interactions through machine learning algorithms, enabling computational efficiency while preserving high fidelity [34].

In this work, we employed machine learning molecular dynamics simulations to systematically elucidate the heat conduction enhancement mechanisms of interconnected diamond/Cu network structures. We constructed comprehensive training datasets encompassing diamond/Cu interfaces with various orientations and atomic mixing configurations based on density functional theory (DFT) calculations, developed an MLP for diamond/Cu heterostructures using the neuroevolution potential (NEP) framework [35], and rigorously validated its accuracy through comparisons with experimental data and DFT benchmarks. Subsequently, we employed the homogeneous non-equilibrium molecular dynamics (HNEMD) method to calculate the lattice thermal conductivity (LTC) of two series of network structures (diamond network/Cu and Cu network/diamond) [36], providing in-depth analysis of the influence of diamond content on the thermal properties of composite materials. Through spectral LTC decomposition, we elucidated the competitive effects between low-frequency Cu phonons and high-frequency diamond phonons. Finally, we employed phonon wave analysis to investigate the underlying physical mechanisms governing thermal transport in these nano-network structures. This study provided theoretical insights and design principles for developing high-performance DMCs.

2. Methods

2.1. Density functional theory calculations

All DFT calculations in this work were performed using the projector augmented wave (PAW) potentials and the Perdew–Burke–Ernzerhof (PBE) form of generalized gradient approximation for the exchange–correlation functional, with a kinetic energy cutoff of 600 eV [37,38]. For geometry optimization of diamond and Cu, a Gamma-centered 14 × 14 × 14 k-point mesh was employed, with electronic energy convergence criteria set to 1×10^{-10} eV and atomic force convergence criterion set to 1×10^{-6} eV/Å. Phonon dispersion relations and group velocities for both materials were calculated using the PHONOPY package combined with the finite displacement method [39,40], where harmonic interatomic force constants were obtained through 4 × 4 × 4

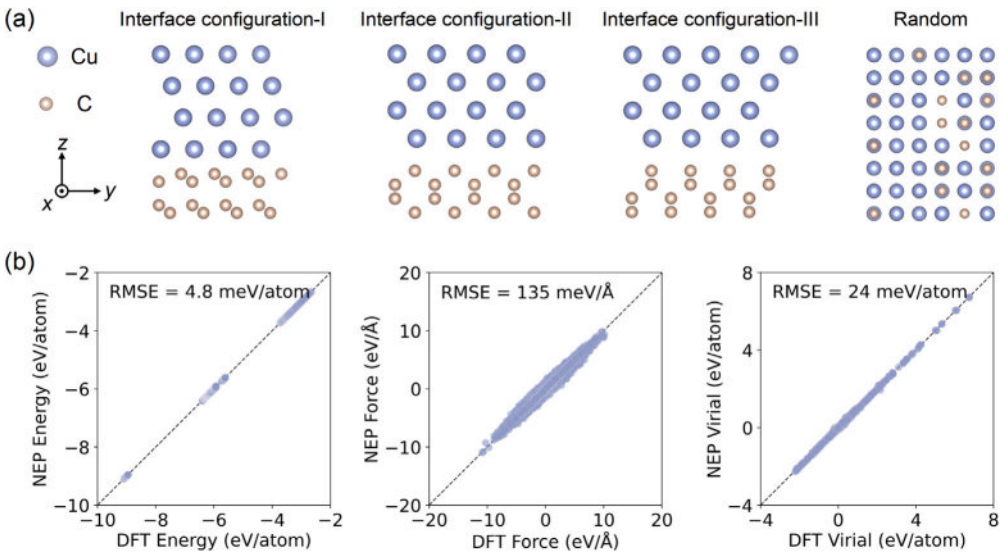

Fig. 2. Dataset construction and training of the NEP model. (a) Representative diamond/Cu heterostructure configurations included in the training dataset. Interface configurations I–III represent different atomic arrangements at the diamond/Cu interface, arising from variations in atomic registry, interfacial bonding patterns, and termination structures, while the "Random" configuration includes randomly mixed C and Cu atoms to capture disordered interfacial regions. (b) Parity plots comparing NEP model predictions with DFT reference data for energy, force, and virial.

supercells with a $3 \times 3 \times 3$ k-point mesh. For static single-point calculations of all structures in the training dataset, to balance computational accuracy and efficiency, the electronic energy convergence criteria were set to 1×10^{-6} eV, and the Brillouin zone was sampled using a Gamma-centered grid with a k-point density of 0.2/Å.

2.2. Training dataset and neuroevolution potential model

As illustrated in Fig. 2a, our training dataset includes pure diamond, pure Cu, as well as diamond/Cu interfaces with distinct atomic configurations and random mixing structures. We constructed three interface models based on different crystallographic orientations (labeled as Interface configuration-I, II, and III): diamond(111)/Cu(111), diamond(010)/Cu(010), and diamond(001)/Cu(001). Although diamond and Cu possess cubic symmetry, the actual interfacial structure depends on the specific atomic registry and bonding environment across the interface. These configurations represent different stacking sequences and local atomic arrangements. Initial structures were obtained through MD simulations combined with the recently released NEP89 universal MLP [41]. This MLP supports 89 chemical elements and can describe complex interactions ranging from covalent bonds to metallic bonds and heterogeneous interfaces. The approach of obtaining initial structures through MD+NEP89 offers significant computational advantages compared to traditional ab initio molecular dynamics (AIMD) methods [42]. Specifically, for each representative structure type shown in Fig. 2a, NPT equilibration at zero pressure was first performed for 1 ns in the temperature range of 100–700 K, followed by 5 ns of NVT sampling, with representative configurations extracted at 0.1 ns sampling intervals throughout both NPT and NVT processes. To increase structural diversity, uniform random strains ranging from −3% to +3% were applied to selected extracted structures, and Gaussian perturbations with a standard deviation of 0.1 Å were added to atomic coordinates. All sampled structures were subsequently subjected to DFT single-point energy calculations using the computational settings described in Section 2.1. Additionally, we integrated validated high-quality Cu DFT data from UNEP-v1, a universal potential for 16 metals [31], and for pure diamond from the dataset reported in Ref. [43]. The final comprehensive training dataset for diamond/Cu comprises 2700 structures.

Using this training dataset, we developed an MLP for diamond/Cu heterostructures based on the NEP model [35]. The NEP model is based on artificial neural networks and trained using the separable natural evolution strategy, demonstrating excellent accuracy and computational efficiency [34]. The NEP model was trained with a radial cutoff distance $r_C^R = 6$ Å and an angular cutoff distance $r_C^A = 5$ Å. The accuracy of the constructed NEP model was validated through comparison with DFT reference calculations, as shown in Fig. 2b. The parity plots demonstrate consistency between NEP predictions and DFT results for all evaluated properties, with root mean square errors (RMSEs) of 4.8 meV/atom, 135 meV/Å, and 24 meV/atom for energy, forces, and virial, respectively. These RMSE values are all within acceptable ranges for high-precision MD simulations, indicating that the trained NEP model can accurately capture the fundamental physical characteristics of diamond/Cu interactions. In subsequent Sections 3.1 and 3.2, we further validated the prediction accuracy of this MLP for thermophysical properties of diamond/Cu systems through calculations of phonon dispersion relations, thermal conductivity, and interfacial thermal conductance.

2.3. Homogeneous nonequilibrium molecular dynamics

We employ the HNEMD method with the trained NEP model to calculate the LTC of diamond, Cu, and their network structures [36]. All HNEMD simulations were performed using the GPUMD software package [42]. This method simulates thermal transport by introducing an external driving force $\mathbf{F}_i^{ext}$ on each atom i [36,44]:

$$\mathbf{F}_i^{ext} = E_i \mathbf{F}_e + \mathbf{F}_e \cdot \mathbf{W}_i, \tag{1}$$

where $\mathbf{F}_e$ has dimensions of inverse length, E_i is the total energy of particle i and $\mathbf{W}_i$ is virial tensor of atom i. The driving force induces a non-equilibrium heat current $\langle \mathbf{J} \rangle_{ne}$ that is linearly related to $\mathbf{F}_e$ in the linear response regime:

$$\frac{\langle J^\mu(t) \rangle_{ne}}{TV} = \sum_\nu \kappa^{\mu\nu} F_e^\nu, \tag{2}$$

where $\kappa^{\mu\nu}$ is the thermal conductivity tensor, T is the system temperature, and V is the system volume.

2.4. Spectral thermal conductivity decomposition

Within the HNEMD framework, it is possible to calculate spectrally decomposed thermal conductivity. The foundation of spectral heat

current decomposition is based on the calculation of the virial-velocity time correlation function, which is defined as [44]:

$$\mathbf{K}(t) = \sum_i \langle \mathbf{W}_i(0) \cdot \mathbf{v}_i(t) \rangle, \tag{3}$$

where $\mathbf{W}_i$ represents the virial tensor of atom i, $\mathbf{v}_i(t)$ is the velocity vector of atom i at time t, and the angular brackets denote ensemble averaging. The spectrally decomposed thermal conductivity can be obtained through the following formula [36]:

$$\kappa(\omega) = \frac{2}{VTF_e} \int_{-\infty}^{\infty} e^{i\omega t} K(t) dt, \tag{4}$$

with

$$\kappa = \int_0^{\infty} \frac{d\omega}{2\pi} \kappa(\omega), \tag{5}$$

where V is the volume of the considered system, F_e is the magnitude of the driving force parameter in the HNEMD method, and $K(t)$ is the virial-velocity correlation function in the transport direction.

3. Results and discussion

3.1. Neuroevolution potential model validation

To verify the accuracy of the trained NEP model in capturing thermal transport properties, we calculated the LTC of diamond and Cu using HNEMD simulations [36]. In the calculations, the driving force parameters F_e were set to 1×10^{-5}/Å and 1×10^{-4}/Å for diamond and Cu, respectively, to ensure the validity of linear response theory. These values were sufficiently small to maintain the linear response regime while being large enough to achieve adequate signal-to-noise ratios. The interatomic interactions in the diamond/Cu systems were described by the trained NEP potential. Periodic boundary conditions were applied in all x, y, and z directions for all structures. The systems were first equilibrated in the NPT ensemble at the target temperature and zero pressure for 1 ns. Subsequently, production runs were performed in the NVT ensemble using Nosé-Hoover chain thermostats to maintain the target temperature, with heat flux data collected for 6 ns using a time step of 1 fs.

As shown in Figs. 3a and 3c, the LTC predicted by MD-NEP simulations in the temperature range of 200–500 K shows good agreement with experimental and computational results from other works [45–51]. Additionally, we calculated the phonon dispersion relations and density of states (DOS) for diamond and Cu using the NEP model, as presented in Figs. 3b and 3d. The NEP results are consistent with DFT reference calculations. The comparison of LTC and phonon spectra validates that the NEP model successfully captures the phonon vibrational characteristics necessary for accurate thermal transport calculations. These computational results confirm the reliability of the trained NEP model for subsequent studies of phonon thermal transport in diamond/Cu network structures.

3.2. Interfacial thermal properties of diamond/Cu

Diamond/Cu network structures contain numerous interfaces where interfacial scattering plays a crucial role in phonon thermal transport, particularly for diamond/Cu interfaces with significant phonon mismatch. To understand the fundamental mechanisms affecting heat transfer across diamond/Cu interfaces, we first analyzed the phonon properties of the constituent materials. As shown in Fig. 4a, the normalized phonon DOS calculated by DFT reveals significant mismatch between diamond and Cu. Diamond exhibits high-frequency optical modes up to ~40 THz due to strong C–C bonds and light atomic mass, while Cu primarily displays low-frequency modes below ~8 THz, which is characteristic of metallic systems. This frequency mismatch constitutes a fundamental barrier for phonon transmission across interfaces.

Phonon group velocity analysis (Fig. 4b) further reveals distinctly different transport characteristics of the two materials. Diamond shows significantly higher group velocities across the entire frequency spectrum, particularly for acoustic modes, reflecting its superior intrinsic LTC. In contrast, Cu exhibits lower and more dispersed group velocities, consistent with its metallic nature and relatively lower LTC compared to diamond. This pronounced group velocity mismatch not only affects phonon transmission at individual interfaces but, more importantly, results in very small critical angles for total internal reflection, causing most wavelike phonons to undergo total internal reflection in multi-interface network structures. This phenomenon will be analyzed in detail through phonon wave equations in Section 3.5.

To quantify the thermal transport properties of diamond/Cu interfaces, we performed non-equilibrium molecular dynamics (NEMD) simulations using the validated NEP MLP [42]. Fig. 4c presents the simulation setup and the corresponding temperature distribution of the system. The constructed interface model employed Cu(111) and Diamond(111) crystal planes with a total system length of 24 nm, including an effective thermal transport length of ~20 nm, fixed layers of ~1 nm at each end, and heat source and heat sink layers of ~1 nm each. The cross-sectional areas of both Cu(111) and Diamond(111) sides were 18 × 18 unit cells (~18.4 nm^2), with a lattice mismatch rate less than 2% at the interface.

The interfacial temperature jump ΔT was extracted using linear extrapolation. Linear temperature profiles in regions far from the interface on both Cu and diamond sides were fitted separately, and the fitting lines were extrapolated to the interface midpoint. The interfacial temperature difference was defined as the difference between the two extrapolated temperatures. Finally, the ITC was calculated using Fourier's law: $G = Q/(A\Delta T)$, where Q is the steady-state heat flux density, A is the interfacial cross-sectional area, and ΔT is the extrapolated interfacial temperature difference.

The temperature-dependent ITC results from MD-NEP simulations are shown in Fig. 4d, demonstrating good agreement with existing experimental measurements and computational studies reported in the literature (300 K) [52–56]. The slight variations among different studies can be attributed to differences in interfacial preparation, surface roughness, and measurement techniques in experiments, or different computational parameters and model choices in theoretical studies. These validations against multiple independent sources further confirm the reliability of the NEP-based approach for predicting interfacial thermal transport in diamond/Cu systems.

3.3. Lattice thermal conductivity and phonon transport of diamond/Cu network structures

To systematically investigate the thermal transport properties of interconnected network structures [17], we constructed two types of periodic nanostructures: diamond networks filled with Cu nanopillars (DN/Cu) and Cu networks filled with diamond nanopillars (CuN/D), as shown in Fig. 5. These two structural types, by interchanging the roles of matrix and nanopillar materials, provide a comparative framework for understanding the influence of diamond discrete versus interconnected structures on LTC performance as illustrated in Fig. 1.

The DN/Cu structure series employs diamond as the continuous network matrix with embedded Cu nanopillars. During the modeling process, a diamond matrix with 12 atomic layers thickness was first constructed based on the (100) crystallographic orientation (10 × 10 supercell expansion in the xy directions), forming a basic periodic unit of 3.57 × 3.57 × 4.2 nm. Subsequently, the geometric dimensions of Cu nanopillars were precisely controlled to systematically cover Cu volume fractions ranging from 10% to 90%. Since the nanopillars extend through the entire thickness of the structure, the area fraction $(L_{dia}/L_{pd})^2$ is equivalent to the volume fraction. Through 3 × 3 array expansion of this periodic unit, the final generated structures

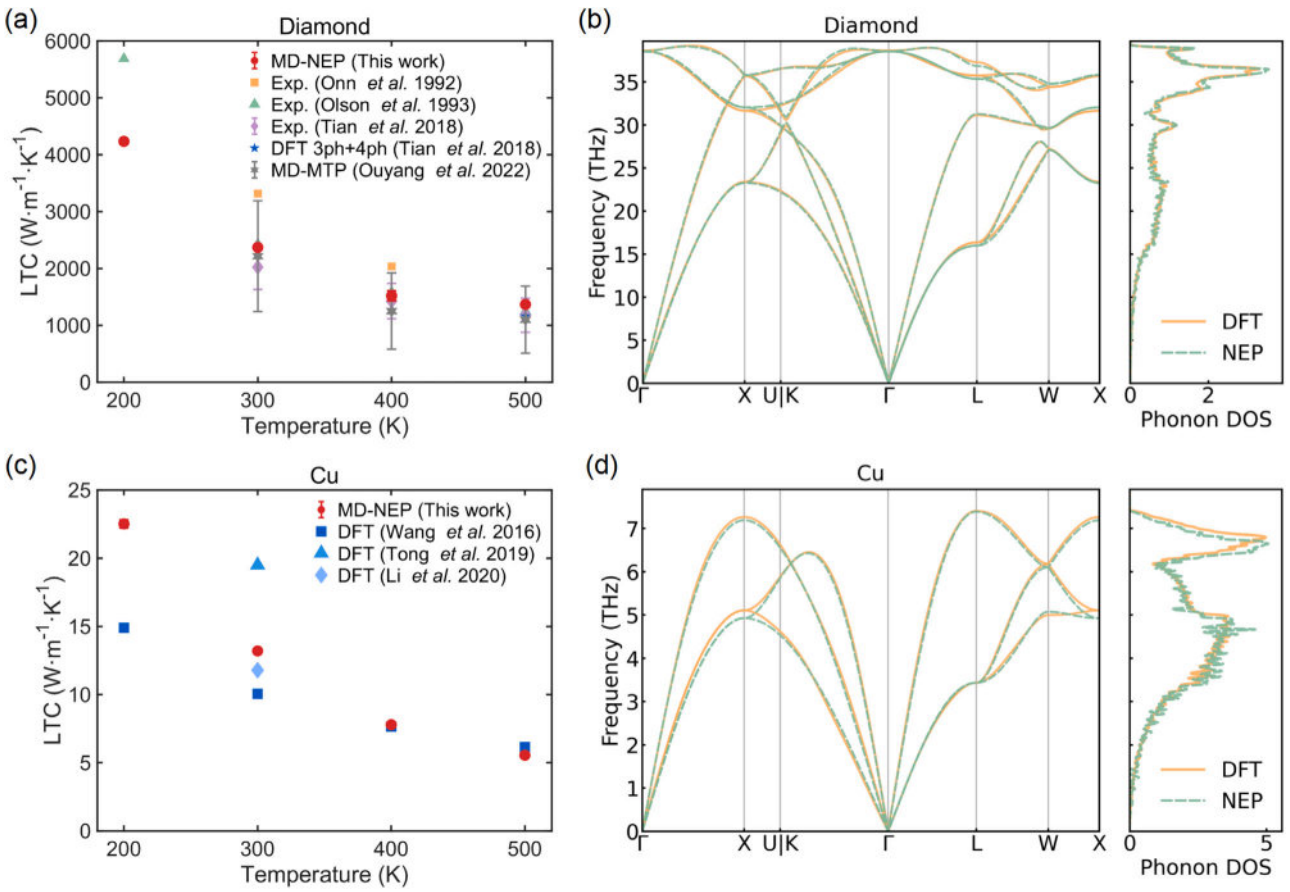

Fig. 3. Validation of the NEP model for thermal transport properties. Temperature-dependent LTC calculated using MD-NEP simulations for (a) diamond and (c) Cu, compared with experimental data [46,47,49] and other computational results [45,48,50,51]. Phonon dispersion relations and DOS calculated using the NEP model (dashed lines) and DFT (solid lines) for (b) diamond and (d) Cu. 3ph+4ph refers to DFT calculations considering three-phonon and four-phonon interactions [49], and MTP denotes moment tensor potential [48].

contain 40,977 to 79,668 atoms, with Cu nanopillar volume fractions of 10.0%–90.2%, corresponding to diamond volume fractions of 9.8%–90.0%, and system dimensions of approximately $10.7 \times 10.7 \times 4.2$ nm^3. The CuN/D structure series adopts the opposite material configuration, using Cu as the continuous matrix with embedded diamond nanopillars. During the construction of the CuN/D structures, special care was taken to address the significant lattice and bonding mismatch between diamond and Cu. To minimize interfacial strain, the diamond lattice was pre-compressed isotropically by 3%–5% to better match the Cu matrix. A thin interfacial buffer zone of approximately 1 Åwidth was introduced, within which Cu atoms were initially placed according to the expanded diamond sublattice positions. However, only 60%–80% of these Cu sites were occupied to prevent atomic overcrowding and allow for structural relaxation. During atomic placement, a minimum interatomic distance of ~2 Åwas enforced to avoid unphysical overlaps. Following similar modeling procedures for periodic unit construction and subsequent 3 × 3 array expansion, this series generates structures with diamond volume fractions of 11.7%–72.8% and system dimensions of approximately $10.9 \times 10.9 \times 4.2$ nm^3.

The (100) crystallographic orientation was selected because this plane represents a low-index stable surface for both Cu and diamond crystals, featuring relatively simple and regular atomic arrangements that help reduce interface mismatch stress, facilitate construction of geometrically regular nanopillar structures, and enable precise control of supercell dimensions and compositional ratios while simplifying modeling complexity. It should be noted that while the overall structure is constructed based on the (100) orientation, at the actual diamond/Cu interfaces, due to atomic relaxation and interface energy optimization, complex interface structures with various local orientations including (111), (010), (001) and others are formed. This interface diversity significantly affects phonon scattering and LTC performance. Therefore, we incorporated diamond/Cu interface structures with different orientations into the training dataset for our NEP model.

By fixing the periodic unit size and number of periods while varying the diamond volume fraction within each periodic unit, we analyzed the influence of structural variations on LTC. The LTC of these structures was calculated across the temperature range of 200–500 K using the HNEMD method [36]. The driving force parameters F_e for DN/Cu and CuN/D structures were selected as 5×10^{-5}/Å and 1×10^{-4}/Å, respectively. Periodic boundary conditions were applied in all x, y, and z directions for all structures. For each structure at each temperature, the systems were first equilibrated in the NPT ensemble at the target temperature and zero pressure for 1 ns. Subsequently, production runs were performed in the NVT ensemble using Nosé–Hoover chain thermostats to maintain the target temperature, with heat flux data collected for 6 ns using a time step of 1 fs.

It is noteworthy that the diamond nanopillars in the CuN/D configuration exhibit reduced crystalline order near the interface after structural relaxation, as shown in Fig. 5(b). This structural perturbation arises from significant lattice mismatch, bonding heterogeneity, and interfacial strain between diamond and Cu. During the MD equilibration process, atomic rearrangement and limited Cu-C mixing occur within a few atomic layers at the interface, leading to local bond distortion and partial loss of tetrahedral coordination in diamond. This effect is more pronounced in CuN/D than in DN/Cu due to the higher surface-to-volume ratio of isolated diamond nanopillars. Such interface-induced

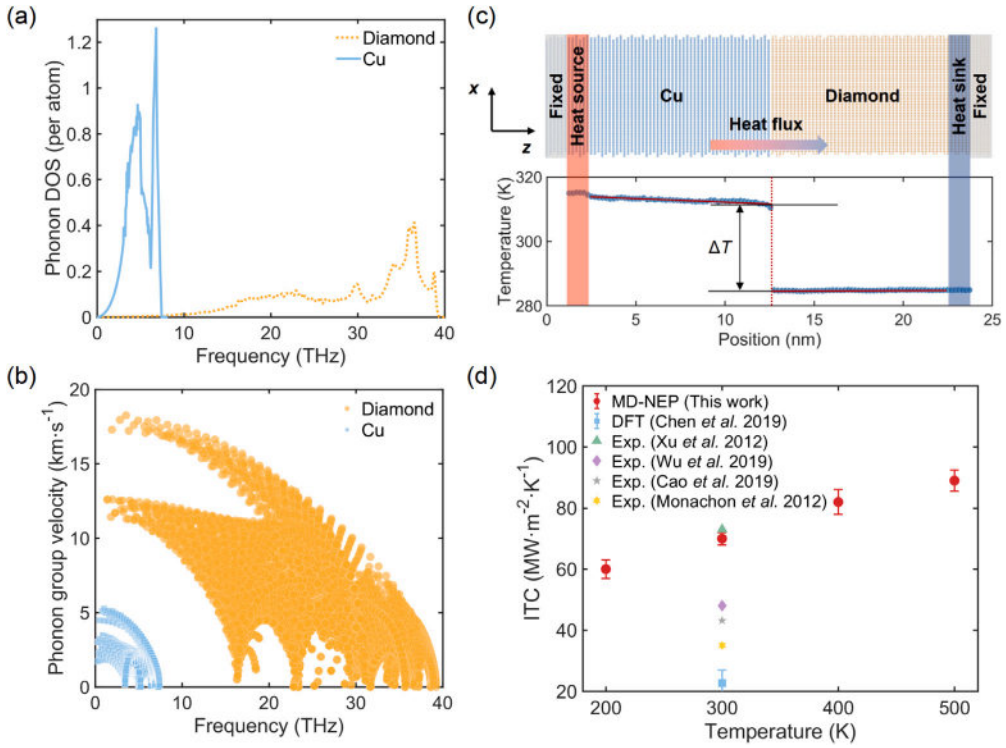

Fig. 4. Phonon properties and interfacial thermal conductance (ITC) of diamond/Cu heterostructures. (a) Normalized phonon DOS (per atom) and (b) group velocities of diamond and Cu calculated using DFT, showing significant phonon mismatch between the two materials. (c) NEMD simulation setup for calculating ITC (top) and corresponding steady-state temperature profile (bottom), with clear temperature jump (ΔT) at the interface. (d) Temperature-dependent ITC calculated using MD-NEP compared with experimental data and other computational results from Refs. [52–56].

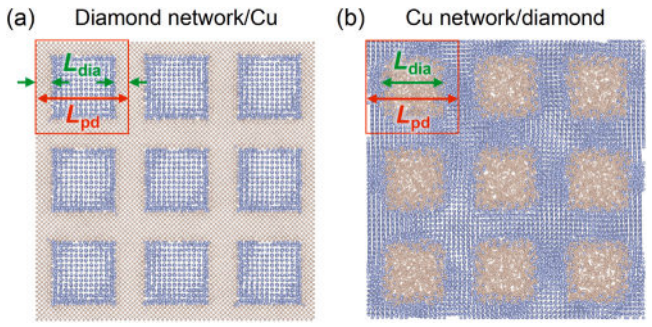

Fig. 5. Schematic diagrams of two periodic structures: (a) diamond network filled with Cu nanopillars and (b) Cu network filled with diamond nanopillars. The figures show equilibrium configurations after MD structural optimization. Geometric parameters L_{dia} and L_{pd} represent the diamond segment length and period length within a single unit cell, respectively, where $L_{pd} = L_{dia} + L_{Cu}$.

structural degradation can enhance phonon scattering, thereby further suppressing thermal conductivity beyond the limitations imposed by the discontinuous network topology.

As shown in Fig. 6a, the two structural types exhibit distinctly different LTC variation trends. The LTC of DN/Cu structures shows a monotonic increasing trend with increasing diamond volume fraction, benefiting from the continuous high heat transfer channels formed by diamond. In contrast, CuN/D structures exhibit more complex non-monotonic behavior. The LTC first decreases with increasing diamond proportion and reaches a minimum value at approximately 50% diamond content. Consequently, Fig. 6a also demonstrates the important phenomenon anticipated in Fig. 1. When the diamond volume fraction exceeds approximately 30%, under identical diamond content conditions, the LTC of DN/Cu structures is consistently and significantly higher than that of CuN/D structures. This difference quantitatively validates the significant advantage of interconnected network design over dispersed filling. In diamond networks, high thermal conductivity diamond forms continuous heat transfer channels, while in Cu networks, diamond is segmented into isolated nanopillars that cannot fully utilize their excellent heat conduction capability. This result provides quantitative theoretical support for the interconnected network design concept illustrated in Fig. 1.

It is noteworthy that diamond networks exhibit better structural stability compared to Cu networks. During MD simulation relaxation, the interface regions of CuN/D structures show more atomic mixing and rearrangement phenomena (Fig. 5). Although moderate atomic mixing helps reduce diamond/Cu interface thermal resistance and enhance interface heat conduction performance [43,57,58], the enhancement effect of interconnected diamond structures on LTC is more significant.

Figs. 6b and 6c present the LTC of both network structure series as a function of diamond content across the temperature range of 200–500 K, revealing distinct temperature-dependent behaviors. For DN/Cu structures (Fig. 6b), the temperature effect on LTC is relatively modest and diminishes progressively with increasing diamond content. This behavior primarily stems from the dominance of the diamond phase at higher concentrations. Given the high Debye temperature of diamond (~2200 K), the occupation of mid-to-high frequency phonon modes remains limited within the 200–500 K range, resulting in relatively weak phonon–phonon scattering. Consequently, the LTC is predominantly governed by the intrinsic thermal transport properties of diamond, exhibiting minimal sensitivity to temperature variations. At lower diamond contents, the increasing contribution from the Cu phase introduces more pronounced temperature dependence, as the lower Debye temperature of Cu (~343 K) renders its phonon scattering more temperature-sensitive. This leads to a slight decrease in overall LTC with increasing temperature, though this reduction diminishes as diamond content increases.

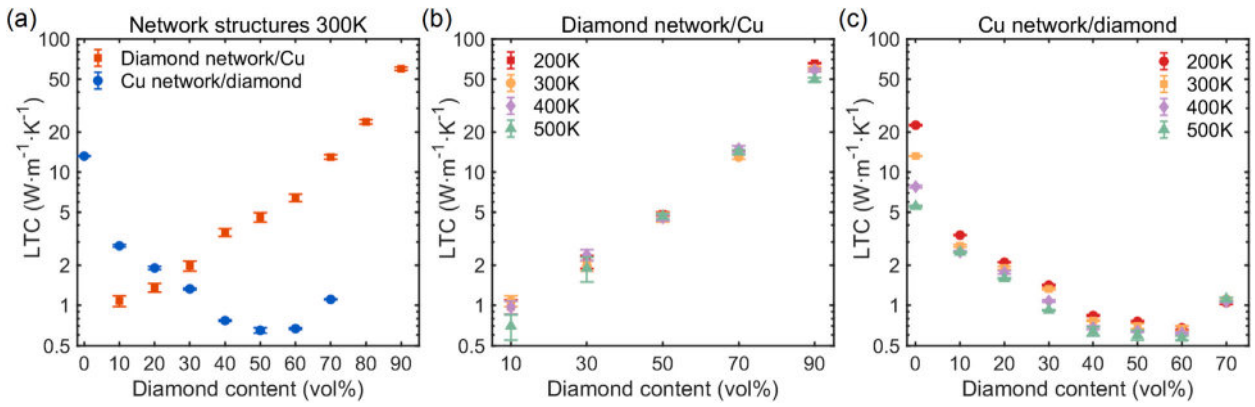

Fig. 6. LTC of two-dimensional diamond/Cu network structures. (a) LTC at 300 K as a function of diamond volume fraction calculated using MD-NEP simulations. The DN/Cu structure (orange squares) shows a monotonic increasing trend, while the CuN/D (blue circles) exhibits non-monotonic behavior with a minimum at diamond volume fraction of approximately 50%. LTC of (b) DN/Cu and (c) CuN/D structure as a function of diamond volume fraction at different temperatures.

In contrast, CuN/D structures (Fig. 6c) exhibit pronounced temperature dependence, dominated by the Cu matrix. The phonons of Cu are primarily concentrated in the low-frequency region (0–8 THz), where phonon occupation increases significantly within the 200–500 K temperature range. This enhancement in phonon–phonon scattering leads to a notable decrease in LTC with rising temperature. Although the contribution from high-frequency diamond phonons (10–40 THz) gradually increases with diamond content, partially offsetting the temperature effect of the Cu phase and reducing the LTC variation across different temperatures, the overall temperature sensitivity remains significant. This persistent temperature dependence arises from the segmented nature of diamond nanopillars, where interfacial scattering severely constrains their thermal transport contribution, preventing effective mitigation of the temperature effect even at elevated diamond contents.

Overall, both structural series demonstrate decreasing LTC trends from 200 K to 500 K, consistent with the temperature dependencies observed in pure diamond and pure Cu (Figs. 3a and 3c). Notably, although the ITC increases with temperature (Fig. 4d), its variation remains relatively modest within the 200–500 K range. The influence of ITC on overall LTC is subordinate to the intrinsic temperature effects of the dominant material phase. Therefore, the temperature dependence of LTC in these composite structures is primarily determined by the volume fraction and intrinsic thermal transport characteristics of the dominant phase—diamond in DN/Cu and Cu in CuN/D structures.

3.4. Spectral lattice thermal conductivity

To elucidate the microscopic origins of the contrasting LTC trends observed in Fig. 6, particularly the monotonic behavior of DN/Cu versus the non-monotonic behavior of CuN/D structures, we calculated the spectral LTC of both structural series using MD-NEP and compared them with the spectral LTC of pure diamond and Cu. As shown in Fig. 7, the LTC of diamond is primarily dominated by high-frequency phonons (10–40 THz), while Cu mainly relies on low-frequency phonons (0–8 THz). The spectral LTC of both materials decreases with increasing temperature due to enhanced phonon–phonon scattering, though the temperature sensitivity differs significantly between the two materials, as will be discussed below.

DN/Cu structures (Figs. 8a–d) exhibit overall increasing spectral LTC with diamond content. The dominant trend is the significantly enhanced contributions from the high-frequency region (10–40 THz), which increase rapidly with diamond volume fraction due to the formation of continuous diamond networks. Contributions from the low-frequency region (0–8 THz) show a slight decline as diamond content increases, reflecting the reduced Cu volume. However, this low-frequency reduction is negligible compared to the high-frequency enhancement, resulting in the monotonic increase in total LTC observed in Fig. 6.

The spectral evolution of CuN/D structures (Figs. 8e–h) presents more complex competitive characteristics. With increasing diamond volume fraction, the contribution of Cu-dominated low-frequency phonons (0–8 THz) rapidly decreases, leading to gradual reduction in total LTC. Due to the dispersed form of diamond in this structure, its contribution to LTC grows slowly compared to interconnected structures. When the contributions of low-frequency Cu phonons and high-frequency diamond phonons gradually approach each other (at approximately 50% diamond content), the competition between them reaches a critical equilibrium point, resulting in the minimum total LTC phenomenon. Subsequently, the contribution of diamond high-frequency phonons (10–40 THz) begins to dominate, driving the total LTC to rise again. In Cu network structures, diamond is segmented into isolated nanopillars, and its LTC contribution is limited by interface scattering, preventing full utilization of the high thermal conductivity of diamond.

To elucidate the evolution of temperature sensitivity with diamond content, Figs. 9 and 10 replot the spectral LTC with temperature as the varying parameter for each composition (reorganizing the data from Fig. 8). This representation enables direct comparison of how temperature affects different frequency components at each diamond volume fraction. For DN/Cu structures (Fig. 9), as diamond content increases from 10% to 90%, the spectral LTC gradually transitions from being dominated by low-frequency Cu phonons (0–8 THz, temperature-sensitive) to being dominated by high-frequency diamond phonons (10–40 THz, temperature-insensitive). At high diamond contents ($\geqslant$ 70%), the spectral curves across the 200–500 K temperature range exhibit nearly complete overlap, confirming that the continuous diamond network endows this structure with exceptional temperature stability.

In contrast, CuN/D structures (Fig. 10) display pronounced temperature dependence even at diamond contents of 60%–70%. Spectral analysis reveals that although the contribution from high-frequency diamond phonons increases, the discrete nature of the diamond phase necessitates frequent thermal transport across temperature-sensitive diamond/Cu interfaces and through the Cu matrix, resulting in decreased overall spectral LTC with rising temperature. This comparison clearly demonstrates that structural topology (continuous vs. discrete) is the key factor determining the temperature stability of thermal transport in composite materials, and that a continuous diamond network is essential for achieving stable thermal conductivity across a wide temperature range.

Furthermore, compared to the relatively smooth spectral distributions of pure diamond and pure Cu, the spectral LTC of network structures exhibits obvious oscillatory characteristics, with local suppression phenomena appearing in certain frequency ranges, similar to energy band gap effects in phononic crystals [59–61]. Although these suppression regions do not completely drop to zero, they can significantly

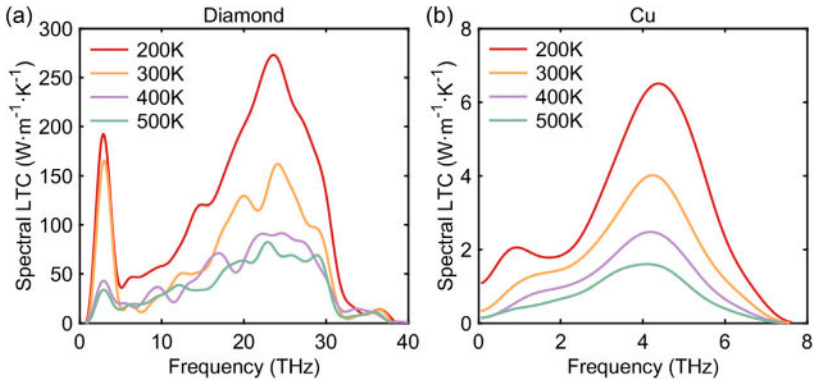

Fig. 7. Spectral LTC of (a) pure diamond and (b) pure Cu at different temperatures calculated using MD-NEP simulations.

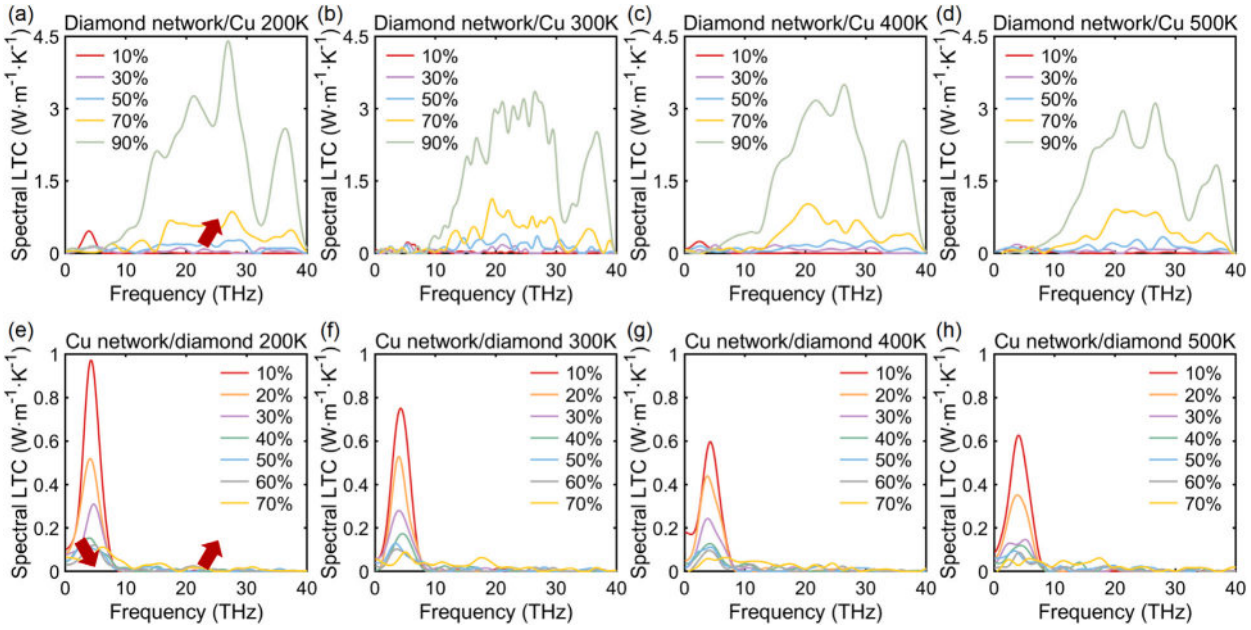

Fig. 8. Spectral LTC of (a)–(d) DN/Cu and (e)–(h) CuN/D structures, showing different diamond volume fractions at various temperatures.

reduce the thermal transport contributions of corresponding frequency phonons. This spectral oscillation phenomenon primarily originates from wavelike interference effects of phonons in the periodically alternating diamond/Cu structures [62–66]. When phonon wavelengths match the periodic characteristic dimensions of the structure, constructive or destructive interference occurs, thereby modulating the spectral LTC distribution.

Despite significant improvements in network structures compared to traditional composite materials with dispersed diamond particles in Cu matrices, their LTC remains much smaller than that of pure diamond, indicating considerable room for design optimization. This is mainly attributed to interface scattering caused by the enormous mismatch in phonon DOS and group velocities between diamond and Cu (Figs. 4a and 4b), as well as complex phonon wavelike effects induced by multiple interfaces in nanonetwork structures. While MD simulations, based on ensemble statistical methods, and spectral LTC analysis can reveal frequency-dependent transport characteristics, they lack direct description of phonon wavelike propagation processes [67]. To gain deeper understanding of these microscopic mechanisms at the phonon mode level [25,68], we further analyze wavelike phonon propagation behavior in network structures through phonon wave equation analysis to obtain intuitive physical insights.

3.5. Wavelike phonon transport in diamond/Cu network structures

Due to the presence of numerous interfaces in nanonetwork structures, wavelike (coherent) phonons undergo multiple reflections and refractions between interfaces, generating interference effects similar to sound or light waves among different phonons, leading to suppression of phonon transport processes. To quantitatively explain this phenomenon, we draw analogies to light wave or sound wave propagation theory, starting from fundamental elastic wave equations to quantify the thermal transport processes of wavelike phonons in DN/Cu structures [69–71]. As illustrated in Fig. 11a, elastic wave theory indicates the existence of three plane wave modes: two transverse waves (distinguished by whether the vibration direction is parallel to the reflecting interface) and one longitudinal wave, namely shear horizontal (SH) wave, shear vertical (SV) wave, and pressure (P) wave [72,73]. Assuming all materials are isotropic, an independent P wave (or SV wave) incident on an interface will, due to energy and momentum conservation constraints of wavelike phonons, produce reflected P and SV waves as well as transmitted P and SV waves, i.e., mode conversion effects occur. When considering wave propagation in multilayer structures (Fig. 11b), incident waves undergo multiple reflections and transmissions in each layer. Since all forward-propagating waves in the same medium have the same exponential factor, they can be combined

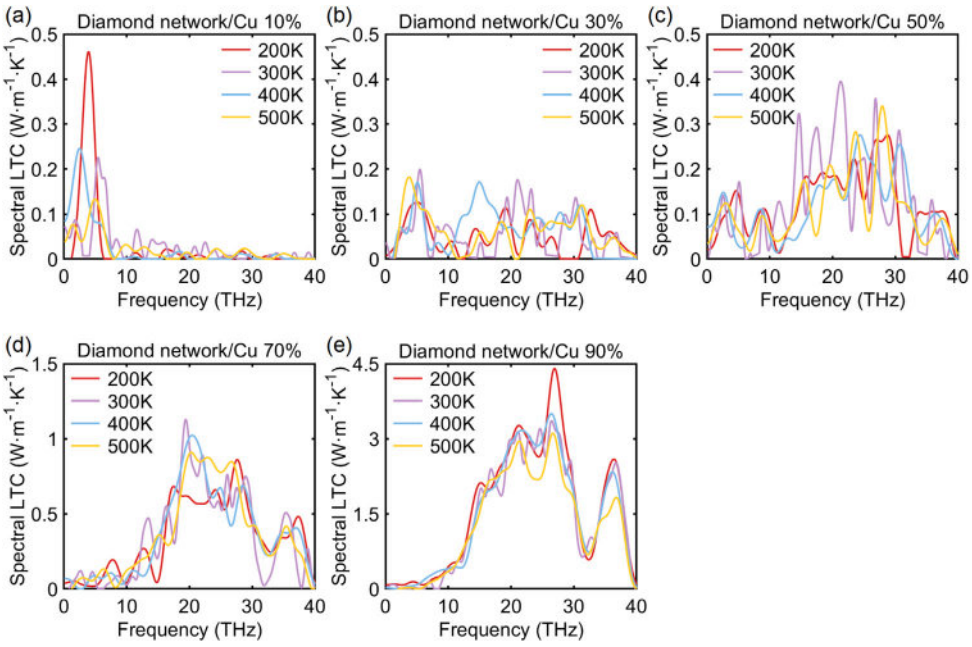

Fig. 9. Spectral LTC of DN/Cu structures at different diamond volume fractions. The data are reorganized from Fig. 8a–d to highlight temperature effects.

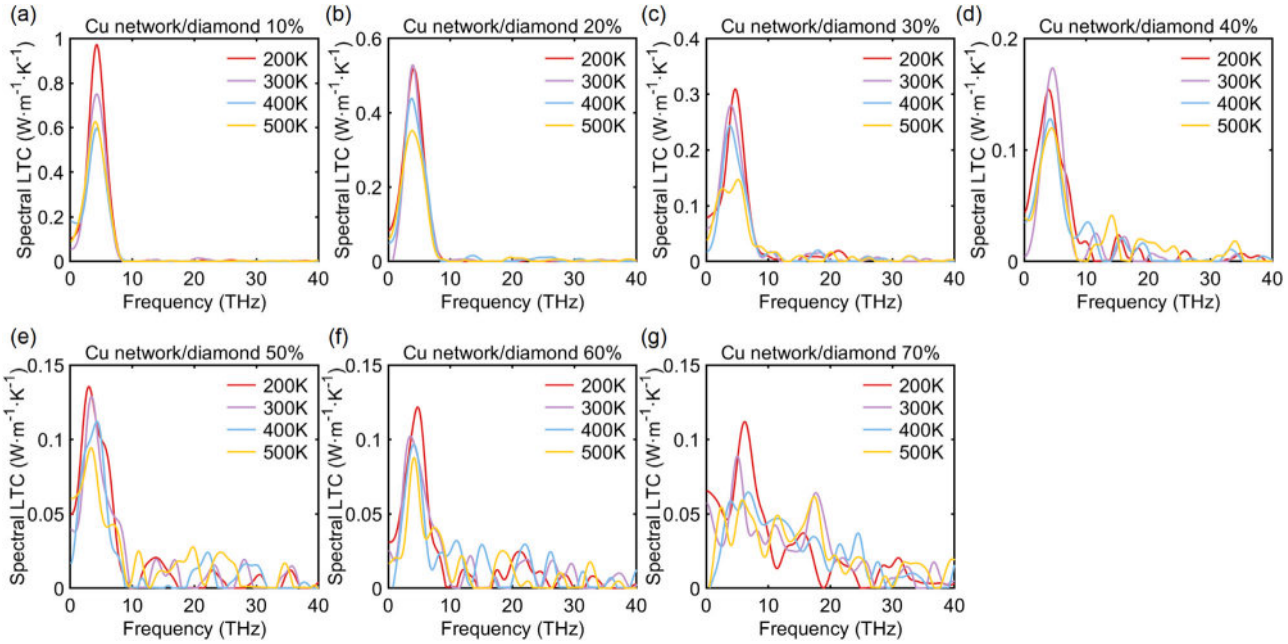

Fig. 10. Spectral LTC of CuN/D structures at different diamond volume fractions. The data are reorganized from Fig. 8e–h to highlight temperature effects.

into a single composite wave with undetermined amplitude. Similarly, we also have a backward-propagating composite wave.

The amplitude of each composite wave is determined by interface boundary conditions, namely the continuity of tangential components of displacement and stress at interfaces. The transfer matrix method is commonly used to relate wave amplitudes between two different positions in multilayer structures. Taking P wave or SV wave incidence on an n-layer multilayer structure as an example, the tangential displacement of propagating waves along the z-axis $U_{j,n}(z) = A_{j,n}e^{izk_z}$ and stress $S_{j,n}(z) = \mu_n \frac{\partial U_{j,n}}{\partial z}$ are continuous at each interface $z = z_n$, where the wave polarization mode $j = tS$ and rS, the first letter represents the excited wave (transmitted t or reflected r) and the second letter represents its polarization (S or P), k_z is the wave vector component in the z-coordinate direction, μ_n is the Lamé constant, and $n = 1, 2, \ldots, 2N + 1$. The amplitudes of the composite transmitted and reflected SV and P waves in the nth layer, $A_{tS,n}$, $A_{tP,n}$, $A_{rS,n}$, and $A_{rP,n}$, can be defined using column vectors as:

$$\mathbf{w}_n = \begin{bmatrix} A_{tS,n} \\ A_{tP,n} \\ A_{rS,n} \\ A_{rP,n} \end{bmatrix}, \tag{6}$$

The continuity conditions of displacement and stress at the interfaces from z_{2N+1} to z_1 are expressed as:

$$\begin{aligned} \mathbf{H}_{2N+2}(z_{2N+1})\mathbf{w}_{2N+2} &= \mathbf{H}_{2N+1}(z_{2N+1})\mathbf{w}_{2N+1}, \\ \mathbf{H}_{2N+1}(z_{2N})\mathbf{w}_{2N+1} &= \mathbf{H}_{2N}(z_{2N})\mathbf{w}_{2N}, \\ &\vdots \end{aligned}$$

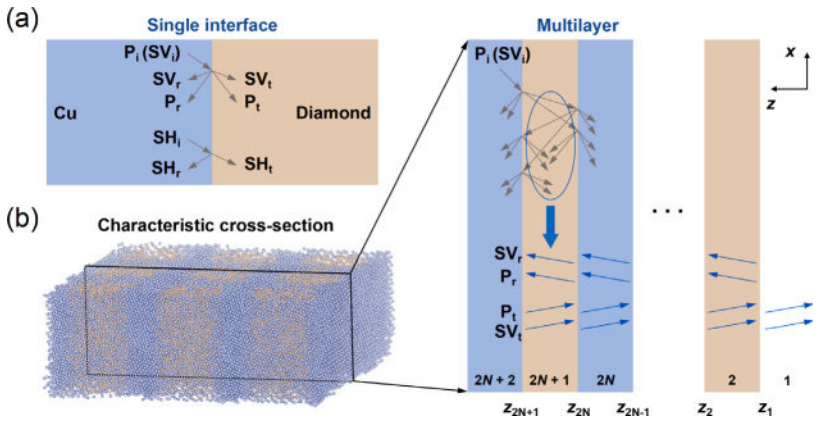

Fig. 11. Schematic illustration of wavelike phonon transport modeling in diamond/Cu network structures. (a) Reflection and transmission of three elastic wave modes (SH, SV, and P waves) at a single interface. (b) Characteristic cross-sectional model along alternating diamond/Cu layers for analyzing multiple reflections and transmissions of wavelike phonons across multiple interfaces.

$$\mathbf{H}_3(z_2)\mathbf{w}_3 = \mathbf{H}_2(z_2)\mathbf{w}_2,$$
$$\mathbf{H}_2(z_1)\mathbf{w}_2 = \mathbf{H}_1(z_1)\mathbf{w}_1, \tag{7}$$

where the 4 × 4 matrix $\mathbf{H}_n(z)$ is the coefficient matrix determined by the continuity conditions of tangential components of displacement and stress at interfaces. According to Eq. (7), we can obtain the relationship between $\mathbf{w}_1$ and $\mathbf{w}_{2N+2}$:

$$\mathbf{w}_1 = \mathbf{T}\mathbf{w}_{2N+2}, \tag{8}$$

where $\mathbf{T} = [\mathbf{H}_1(z_1)]^{-1}\mathbf{H}_2(z_1)\cdots[\mathbf{H}_{2N+1}(z_{2N+1})]^{-1}\mathbf{H}_{2N+2}(z_{2N+1})$ is the so-called transfer matrix. By solving Eq. (8), the amplitude ratio of transmitted waves to incident waves through the entire system can be obtained. The energy flux density of waves is given by:

$$\eta_{j,n} = \frac{1}{2}\rho_n\omega^2 v_{g,j,n}A_{j,n}^2, \tag{9}$$

where ρ_n is the material density and $v_{g,j,n}$ is the group velocity. Using the transfer matrix method, the energy transmission coefficient α_j of multilayer structures can be conveniently calculated, defined as the proportion of incident wave energy flux transmitted into the substrate. The transmission coefficients for incident SV or P waves include contributions from both polarized transmitted waves in the substrate [70]:

$$\alpha_{SV} = \frac{\rho_1 v_{g,S,1}\cos\theta_{tS,1}}{\rho_{2N+2}v_{g,S,2N+2}\cos\theta_{iS,2N+2}}\left(\frac{A_{tS,1}}{A_{iS,2N+2}}\right)^2 + \frac{\rho_1 v_{g,P,1}\cos\theta_{tP,1}}{\rho_{2N+2}v_{g,S,2N+2}\cos\theta_{iS,2N+2}}\left(\frac{A_{tP,1}}{A_{iS,2N+2}}\right)^2, \tag{10}$$

$$\alpha_P = \frac{\rho_1 v_{g,S,1}\cos\theta_{tS,1}}{\rho_{2N+2}v_{g,P,2N+2}\cos\theta_{iP,2N+2}}\left(\frac{A_{tS,1}}{A_{iP,2N+2}}\right)^2 + \frac{\rho_1 v_{g,P,1}\cos\theta_{tP,1}}{\rho_{2N+2}v_{g,P,2N+2}\cos\theta_{iP,2N+2}}\left(\frac{A_{tP,1}}{A_{iP,2N+2}}\right)^2. \tag{11}$$

where $\theta_{j,n}$ is the angle between the corresponding wave propagation direction in the corresponding layer and the interface normal, i.e., incident angle, reflection angle, or transmission angle. It should be noted that the group velocities used here and the phase velocities used in Eq. (7) are determined by the phonon dispersion relations (Figs. 3b and 3d) and are frequency-dependent. For each frequency ω, we have group velocity $v_{g,j}(\omega) = \frac{\partial\omega}{\partial k}$ and phase velocity $v_{p,j}(\omega) = \frac{\omega}{k}$. The transmission coefficient of the system is determined by this method and depends on phonon polarization, frequency, and angle of incidence.

Using the isotropic approximation and considering only the contribution of acoustic phonons, we calculated the phonon transmission coefficients for single diamond/Cu interfaces and multilayer structures (10 layers, alternating diamond and Cu arrangement, each layer thickness of 5 nm), as shown in Fig. 12. Compared to single interfaces, the transmission coefficients of diamond/Cu multilayer structures become lower and form several band gaps. The formation of these band gaps directly corresponds to destructive interference of wavelike phonons between multilayer interfaces [74]. Furthermore, due to the significant group velocity mismatch between diamond and Cu (Fig. 4b), the critical angle for total internal reflection $\theta_c = \arcsin\left(\frac{v_{Cu}}{v_{diamond}}\right)$ becomes very small, producing extensive total internal reflection even at moderate incident angles. Consequently, most wavelike phonons are converted to surface waves propagating along interfaces and gradually dissipating, rather than crossing interfaces to contribute to thermal transport perpendicular to the interface direction.

As shown in Fig. 12, phonon interference and total internal reflection significantly reduce transmission coefficients and thus thermal transport [69–71]. Additionally, when layer thicknesses are at nanoscale approaching or smaller than phonon wavelengths, several evanescent waves can transfer partial energy to the next layer through tunneling, causing partial recovery of the LTC. However, overall, the combined effects of various wave phenomena result in such nanoscale multilayers showing significant enhancement in thermal transport compared to composite materials with diamond particles added to Cu matrices, but still far from reaching the magnitude of pure diamond LTC. The calculation results also demonstrate the important role and enormous potential of nanostructure geometric design, particularly interfaces and period thickness, for LTC enhancement.

The interatomic potentials of MD inherently consider harmonic and various orders of anharmonic terms of phonons, including processes such as phonon interface scattering (Fig. 4), wavelike transport (Fig. 12), and phonon–phonon scattering, and can well predict the LTC of such complex diamond/Cu nanostructures. Combined with MLPs that allow consideration of larger-scale systems with relatively accurate atomic details, they lack mode-level deep understanding of underlying mechanisms, while methods such as phonon wave equations and Green's functions can provide good complementation in this aspect.

It should be noted that the LTC reported in this work is derived from MD simulations and phonon wave analysis, which capture only phonon-mediated heat transport. In Cu, electronic contributions to heat conduction can be significant and are commonly estimated using the Wiedemann–Franz (W–F) law in conjunction with electrical conductivity measurements. The total thermal conductivity of the composite is therefore expected to include both the lattice component obtained from simulations and an additional electronic contribution. In nanostructured composites, interfacial effects such as electron–phonon coupling and boundary scattering may influence the thermal transport behavior, and these factors should be considered when applying the W–F law to

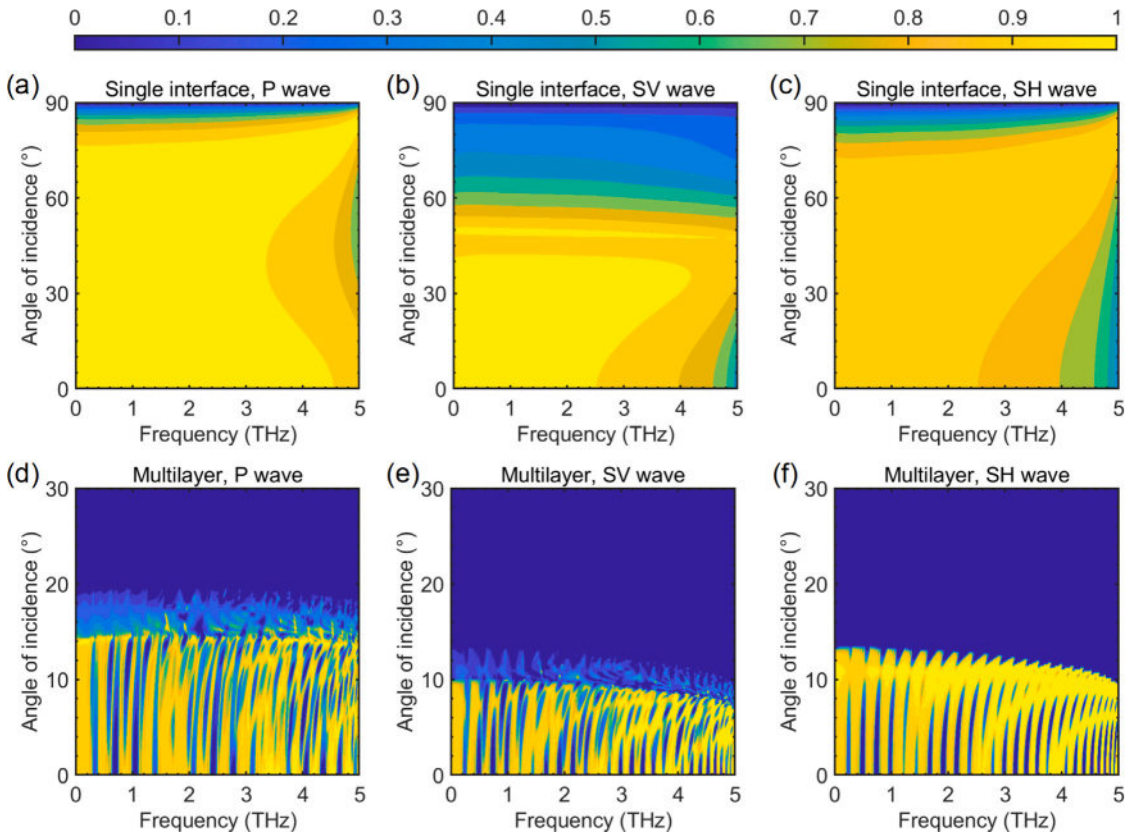

Fig. 12. Phonon transmission coefficients for diamond/Cu (a)–(c) single interface and (d)–(f) multilayer structures, when P wave, SV wave, and SH wave incident, respectively. Transmission coefficient values are represented by color scale (ranging from 0 to 1) depending on phonon polarization, frequency, and angle of incidence.

predict electronic thermal conductivity. Additionally, electron–phonon interactions at the diamond/Cu interface could contribute to interfacial energy transfer, potentially complementing phonon-based conduction mechanisms.

4. Conclusions

This study employs machine learning molecular dynamics simulations to systematically elucidate the phonon heat conduction enhancement mechanisms in diamond/Cu composites with interconnected network structures. By constructing a comprehensive training dataset containing various interface orientations and atomic mixing configurations, we developed a high-accuracy NEP-based MLP for diamond/Cu heterostructures, achieving reliable predictions of thermal transport properties in diamond/Cu heterogeneous interfaces and complex nanostructures.

The significant phonon DOS and group velocity mismatch between diamond and Cu results in substantial interfacial thermal resistance, which constitutes the primary bottleneck limiting overall thermal conductivity enhancement. Through systematic comparison between DN/Cu and CuN/D structures, we validated the remarkable advantages of interconnected diamond networks over conventional particle-reinforced DMCs. When the diamond volume fraction exceeds approximately 30%, the LTC of interconnected diamond structures significantly surpasses that of dispersed structures at equivalent diamond content, effectively reducing interfacial scattering effects by establishing continuous high-conductivity channels and achieving substantial heat conduction performance enhancement.

Furthermore, the LTC of DN/Cu structures exhibits a monotonic increasing trend with diamond content, while CuN/D structures demonstrate a decrease-then-increase pattern with minimum LTC occurring at a diamond volume fraction of approximately 50%. Spectral LTC decomposition reveals that this minimum LTC phenomenon primarily results from the competitive mechanism between low-frequency Cu phonons (0–8 THz) and high-frequency diamond phonons (10–40 THz) contributions to total LTC. Meanwhile, the spectral LTC of network structures exhibits pronounced oscillatory characteristics, manifesting phononic crystal-like energy bandgap effects, which are primarily attributed to coherent interference phenomena of phonons in periodic structures.

To further understand why diamond network structures show significant LTC enhancement yet remain substantially lower than pure diamond, we employed phonon wave equations to analyze the complex propagation behavior of wavelike phonons in nanonetwork structures at the mode level. The analysis demonstrates that phonon interference effects between multilayer interfaces create distinct spectral bandgap features, significantly suppressing thermal transport within specific frequency ranges. Simultaneously, due to the enormous group velocity mismatch between diamond and Cu, the critical angle for total internal reflection becomes very small, causing most incident phonons to undergo total internal reflection rather than effectively contributing to heat conduction. Consequently, substantial design optimization potential remains for such structures.

These findings provide crucial design guidance for optimizing DMCs through controlled microstructural engineering, particularly regarding interfacial density management and geometric parameter optimization. The developed machine learning molecular dynamics approach offers a powerful computational framework for predicting thermal properties of complex nanostructured materials and accelerating the development of next-generation thermal management solutions.

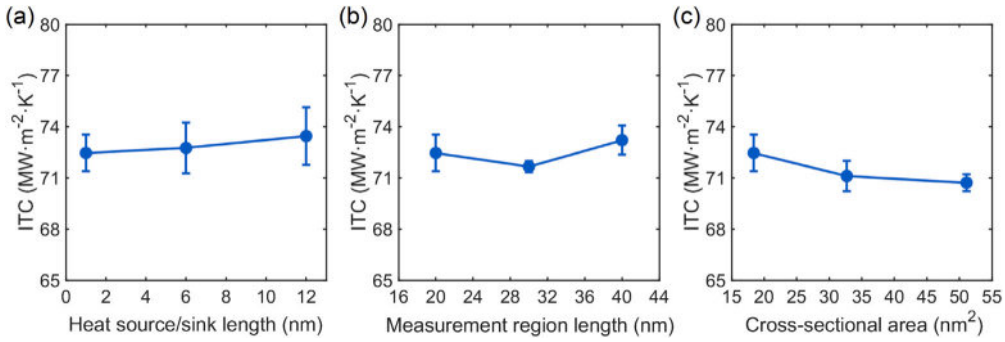

Fig. 13. Calculated ITC values as a function of (a) heat source/sink length, (b) measurement region length, and (c) cross-sectional area at 300 K.

CRediT authorship contribution statement

Bin Liu: Writing – original draft, Software, Investigation. **Zhiguo Tian:** Validation. **Alexander A. Barinov:** Writing – review & editing, Resources. **Moran Wang:** Writing – review & editing, Supervision, Methodology, Conceptualization.

Declaration of competing interest

The authors declare that they have no known competing financial interests or personal relationships that could have appeared to influence the work reported in this paper.

Acknowledgments

This work is financially supported by the Beijing Natural Science Foundation (Grant No. 3254051) and the China Postdoctoral Science Foundation (Grant No. 2023M741895). The calculations are performed on the "Explorer 1000" high-performance computing cluster at the High-Performance Computing Center of Tsinghua University.

Appendix. Convergence tests for interfacial thermal conductance calculations

To ensure the reliability of the ITC calculations, we performed convergence tests with respect to three critical simulation parameters: heat source/sink length, measurement region length, and cross-sectional area. These parameters can significantly influence the computed ITC values in NEMD simulations. These convergence tests indicate that the ITC values reported in the main text are reasonably converged with respect to the key simulation parameters (see Fig. 13).

Data availability

The training dataset will be made freely available at https://github.com/binliu93/Data_for_diamond-Cu.

References

[1] Z. Yan, W. Tong, X. Wang, D. Fan, A review of diamond composites for heat spreaders, Compos. Part A: Appl. Sci. Manuf. 196 (2025) 109008, http://dx.doi.org/10.1016/j.compositesa.2025.109008.

[2] P. Zhu, P. Wang, P. Shao, X. Lin, Z. Xiu, Q. Zhang, E. Kobayashi, G. Wu, Research progress in interface modification and thermal conduction behavior of diamond/metal composites, Int. J. Miner. Met. Mater. 29 (2) (2022) 200–211, http://dx.doi.org/10.1007/s12613-021-2339-6.

[3] Z. Hu, B. Zhang, H. Yu, Y. Lei, H. Xiong, B. Jiang, D. Chen, Research progress of interfacial modification of copper/diamond composites for electronic packaging, Int. J. Thermophys. 46 (9) (2025) 130, http://dx.doi.org/10.1007/s10765-025-03600-x.

[4] H.J. Cho, D. Yan, J. Tam, U. Erb, Effects of diamond particle size on the formation of copper matrix and the thermal transport properties in electrodeposited copper-diamond composite materials, J. Alloys Compd. 791 (2019) 1128–1137, http://dx.doi.org/10.1016/j.jallcom.2019.03.347.

[5] S. Jia, J. Ma, L. Bolzoni, F. Yang, Understanding on the correlation between mechanical properties and thermal conductivity of hot-forged copper/diamond composites, Adv. Eng. Mater. 26 (24) (2024) 2401909, http://dx.doi.org/10.1002/adem.202401909.

[6] H. Li, C. Wang, W. Ding, L. Wu, J. Wang, T. Wei, J. Hu, C. Wu, M. Chen, H. Zhang, T. Lin, W. Liao, Microstructure evolution of diamond with molybdenum coating and thermal conductivity of diamond/copper composites fabricated by spark plasma sintering, J. Mater. Sci., Mater. Electron. 33 (19) (2022) 15369–15384, http://dx.doi.org/10.1007/s10854-022-08441-0.

[7] S. Cui, F. Sun, D. Wang, X. Zhang, H. Zhang, Y. Feng, Enhancing interfacial heat conduction in diamond-reinforced copper composites with boron carbide interlayers for thermal management, Compos. Part B: Eng. 287 (2024) 111871, http://dx.doi.org/10.1016/j.compositesb.2024.111871.

[8] X. Liu, F. Sun, W. Wang, J. Zhao, L. Wang, Z. Che, G. Bai, X. Wang, J. Wang, M.J. Kim, H. Zhang, Effect of chromium interlayer thickness on interfacial thermal conductance across copper/diamond interface, Int. J. Miner. Met. Mater. 29 (11) (2022) 2020–2031, http://dx.doi.org/10.1007/s12613-021-2336-9.

[9] J. Sang, L. Zhou, W. Yang, J. Zhu, L. Fu, D. Li, Enhanced thermal conductivity of copper/diamond composites by fine-regulating microstructure of interfacial tungsten buffer layer, J. Alloys Compd. 856 (2021) 157440, http://dx.doi.org/10.1016/j.jallcom.2020.157440.

[10] R. Liu, G. Luo, Y. Li, J. Zhang, Q. Shen, L. Zhang, Microstructure and thermal properties of diamond/copper composites with Mo2C in-situ nano-coating, Surf. Coat. Technol. 360 (2019) 376–381, http://dx.doi.org/10.1016/j.surfcoat.2018.12.116.

[11] A.V. Ukhina, D.V. Dudina, M.A. Esikov, D.A. Samoshkin, S.V. Stankus, I.N. Skovorodin, E.N. Galashov, B.B. Bokhonov, The influence of morphology and composition of metal–carbide coatings deposited on the diamond surface on the properties of copper–diamond composites, Surf. Coat. Technol. 401 (2020) 126272, http://dx.doi.org/10.1016/j.surfcoat.2020.126272.

[12] C. Azina, I. Cornu, J.-F. Silvain, Y. Lu, J.-L. Battaglia, Effect of titanium and zirconium carbide interphases on the thermal conductivity and interfacial heat transfers in copper/diamond composite materials, AIP Adv. 9 (5) (2019) 055315, http://dx.doi.org/10.1063/1.5052307.

[13] Y. Cao, B. Li, L. Liu, S. Li, D. Hui, S. Wang, H. Liu, X. Li, X. Zhang, S. Zhou, S. Li, Quantitative control of interfacial structure and thermal conductivity between diamond and copper via thermal diffusion of alloying element, J. Mater. Res. Technol. 33 (2024) 6641–6655, http://dx.doi.org/10.1016/j.jmrt.2024.10.250.

[14] L. Wang, J. Li, L. Gao, X. Wang, K. Xu, H. Zhang, J. Wang, M.J. Kim, Gradient interface formation in cu–cr/diamond(ti) composites prepared by gas pressure infiltration, Vacuum 206 (2022) 111549, http://dx.doi.org/10.1016/j.vacuum.2022.111549.

[15] Z. Qi, Y. Zheng, J. Wei, X. Yu, X. Jia, J. Liu, L. Chen, J. Miao, C. Li, Surface treatment of an applied novel all-diamond microchannel heat sink for heat transfer performance enhancement, Appl. Therm. Eng. 177 (2020) 115489, http://dx.doi.org/10.1016/j.applthermaleng.2020.115489.

[16] F.-T. Zohora, M.R. Haque, M.M. Haque, Numerical investigation of the hydrothermal performance of novel pin-fin heat sinks with hyperbolic, wavy, and crinkle geometries and various perforations, Int. J. Therm. Sci. 194 (2023) 108578, http://dx.doi.org/10.1016/j.ijthermalsci.2023.108578.

[17] L. Zhang, Q. Wei, J. An, L. Ma, K. Zhou, W. Ye, Z. Yu, X. Gan, C.-T. Lin, J. Luo, Construction of 3D interconnected diamond networks in al-matrix composite for high-efficiency thermal management, Chem. Eng. J. 380 (2020) 122551, http://dx.doi.org/10.1016/j.cej.2019.122551.

[18] H. Bao, J. Chen, X. Gu, B. Cao, A review of simulation methods in micro/nanoscale heat conduction, ES Energy Environ. 1 (2018) 16–55, http://dx.doi.org/10.30919/esee8c149.

[19] J. Chen, J. He, D. Pan, X. Wang, N. Yang, J. Zhu, S.A. Yang, G. Zhang, Emerging theory and phenomena in thermal conduction: A selective review, Sci. China Phys. Mech. Astron. 65 (11) (2022) 117002, http://dx.doi.org/10.1007/s11433-022-1952-3.

[20] J. Chen, X. Xu, J. Zhou, B. Li, Interfacial thermal resistance: Past, present, and future, Rev. Modern Phys. 94 (2) (2022) 025002, http://dx.doi.org/10.1103/RevModPhys.94.025002.

[21] X. Gu, Z. Fan, H. Bao, Thermal conductivity prediction by atomistic simulation methods: Recent advances and detailed comparison, J. Appl. Phys. 130 (21) (2021) 210902, http://dx.doi.org/10.1063/5.0069175.

[22] B. Liu, V.I. Khvesyuk, A.A. Barinov, M. Wang, Effect of interfacial roughness on thermal boundary conductance: An elastic wave model using the Kirchhoff approximation, Int. J. Mech. Sci. 218 (2022) 106993, http://dx.doi.org/10.1016/j.ijmecsci.2021.106993.

[23] B. Liu, V.I. Khvesyuk, Analytical model for thermal boundary conductance based on elastic wave theory, Int. J. Heat Mass Transfer 159 (2020) 120117, http://dx.doi.org/10.1016/j.ijheatmasstransfer.2020.120117.

[24] X. Wan, W. Feng, Y. Wang, H. Wang, X. Zhang, C. Deng, N. Yang, Materials discovery and properties prediction in thermal transport via materials informatics: A mini review, Nano Lett. 19 (6) (2019) 3387–3395, http://dx.doi.org/10.1021/acs.nanolett.8b05196.

[25] Z. Zhang, Y. Guo, M. Bescond, J. Chen, M. Nomura, S. Volz, Coherent thermal transport in nano-phononic crystals: An overview, APL Mater. 9 (8) (2021) 081102, http://dx.doi.org/10.1063/5.0059024.

[26] Y. Guo, Z. Zhang, M. Bescond, S. Xiong, M. Nomura, S. Volz, Anharmonic phonon-phonon scattering at the interface between two solids by nonequilibrium green's function formalism, Phys. Rev. B 103 (17) (2021) 174306, http://dx.doi.org/10.1103/PhysRevB.103.174306.

[27] Y. Guo, Z. Zhang, M. Nomura, S. Volz, M. Wang, Phonon vortex dynamics in graphene ribbon by solving Boltzmann transport equation with ab initio scattering rates, Int. J. Heat Mass Transfer 169 (2021) 120981, http://dx.doi.org/10.1016/j.ijheatmasstransfer.2021.120981.

[28] W. Miao, M. Wang, Reexamination of electron-phonon coupling constant in continuum model by comparison with Boltzmann transport theory, Int. J. Heat Mass Transfer 174 (2021) 121309, http://dx.doi.org/10.1016/j.ijheatmasstransfer.2021.121309.

[29] X. Ran, Y. Huang, M. Wang, A hybrid Monte Carlo-discrete ordinates method for phonon transport in micro/nanosystems with rough interfaces, Int. J. Heat Mass Transfer 201 (2023) 123624, http://dx.doi.org/10.1016/j.ijheatmasstransfer.2022.123624.

[30] R. Jacobs, D. Morgan, S. Attarian, J. Meng, C. Shen, Z. Wu, C.Y. Xie, J.H. Yang, N. Artrith, B. Blaiszik, G. Ceder, K. Choudhary, G. Csanyi, E.D. Cubuk, B. Deng, R. Drautz, X. Fu, J. Godwin, V. Honavar, O. Isayev, A. Johansson, B. Kozinsky, S. Martiniani, S.P. Ong, I. Poltavsky, K.J. Schmidt, S. Takamoto, A.P. Thompson, J. Westermayr, B.M. Wood, A practical guide to machine learning interatomic potentials – status and future, Curr. Opin. Solid State Mater. Sci. 35 (2025) 101214, http://dx.doi.org/10.1016/j.cossms.2025.101214.

[31] K. Song, R. Zhao, J. Liu, Y. Wang, E. Lindgren, Y. Wang, S. Chen, K. Xu, T. Liang, P. Ying, N. Xu, Z. Zhao, J. Shi, J. Wang, S. Lyu, Z. Zeng, S. Liang, H. Dong, L. Sun, Y. Chen, Z. Zhang, W. Guo, P. Qian, J. Sun, P. Erhart, T. Ala-Nissila, Y. Su, Z. Fan, General-purpose machine-learned potential for 16 elemental metals and their alloys, Nat. Commun. 15 (1) (2024) 10208, http://dx.doi.org/10.1038/s41467-024-54554-x.

[32] P. Ying, C. Qian, R. Zhao, Y. Wang, K. Xu, F. Ding, S. Chen, Z. Fan, Advances in modeling complex materials: The rise of neuroevolution potentials, Chem. Phys. Rev. 6 (1) (2025) 011310, http://dx.doi.org/10.1063/5.0259061.

[33] H. Zhang, X. Gu, Z. Fan, H. Bao, Vibrational anharmonicity results in decreased thermal conductivity of amorphous HfO2 at high temperature, Phys. Rev. B 108 (4) (2023) 045422, http://dx.doi.org/10.1103/PhysRevB.108.045422.

[34] X. Zhou, Y. Liu, B. Tang, J. Wang, H. Dong, X. Xiu, S. Chen, Z. Fan, Million-atom heat transport simulations of polycrystalline graphene approaching first-principles accuracy enabled by neuroevolution potential on desktop GPUs, J. Appl. Phys. 137 (1) (2025) 014305, http://dx.doi.org/10.1063/5.0244987.

[35] Z. Fan, Z. Zeng, C. Zhang, Y. Wang, K. Song, H. Dong, Y. Chen, T. Ala-Nissila, Neuroevolution machine learning potentials: Combining high accuracy and low cost in atomistic simulations and application to heat transport, Phys. Rev. B 104 (10) (2021) 104309, http://dx.doi.org/10.1103/PhysRevB.104.104309.

[36] Z. Fan, H. Dong, A. Harju, T. Ala-Nissila, Homogeneous nonequilibrium molecular dynamics method for heat transport and spectral decomposition with many-body potentials, Phys. Rev. B 99 (6) (2019) 064308, http://dx.doi.org/10.1103/PhysRevB.99.064308.

[37] P.E. Blöchl, Projector augmented-wave method, Phys. Rev. B 50 (24) (1994) 17953–17979, http://dx.doi.org/10.1103/PhysRevB.50.17953.

[38] J.P. Perdew, K. Burke, M. Ernzerhof, Generalized gradient approximation made simple, Phys. Rev. Lett. 77 (18) (1996) 3865–3868, http://dx.doi.org/10.1103/PhysRevLett.77.3865.

[39] A. Togo, First-principles phonon calculations with phonopy and phono3py, J. Phys. Soc. Japan 92 (1) (2023) 012001, http://dx.doi.org/10.7566/JPSJ.92.012001.

[40] A. Togo, L. Chaput, T. Tadano, I. Tanaka, Implementation strategies in phonopy and phono3py, J. Phys.: Condens. Matter. 35 (35) (2023) 353001, http://dx.doi.org/10.1088/1361-648X/acd831.

[41] T. Liang, K. Xu, E. Lindgren, Z. Chen, R. Zhao, J. Liu, B. Tang, B. Zhang, Y. Wang, K. Song, P. Ying, H. Dong, S. Chen, P. Erhart, Z. Fan, T. Ala-Nissila, J. Xu, NEP89: Universal neuroevolution potential for inorganic and organic materials across 89 elements, 2025, ArXiv Preprint.

[42] K. Xu, H. Bu, S. Pan, E. Lindgren, Y. Wu, Y. Wang, J. Liu, K. Song, B. Xu, Y. Li, T. Hainer, L. Svensson, J. Wiktor, R. Zhao, H. Huang, C. Qian, S. Zhang, Z. Zeng, B. Zhang, B. Tang, Y. Xiao, Z. Yan, J. Shi, Z. Liang, J. Wang, T. Liang, S. Cao, Y. Wang, P. Ying, N. Xu, C. Chen, Y. Zhang, Z. Chen, X. Wu, W. Jiang, E. Berger, Y. Li, S. Chen, A.J. Gabourie, H. Dong, S. Xiong, N. Wei, Y. Chen, J. Xu, F. Ding, Z. Sun, T. Ala-Nissila, A. Harju, J. Zheng, P. Guan, P. Erhart, J. Sun, W. Ouyang, Y. Su, Z. Fan, GPUMD 4.0: A high-performance molecular dynamics package for versatile materials simulations with machine-learned potentials, Mater. Genome Eng. Adv. n/a (n/a) (2025) e70028, http://dx.doi.org/10.1002/mgea.70028.

[43] X. Wang, X. Wu, P. Ying, Z. Fan, H. Sun, Interface phonon modes governing the ideal limit of thermal transport across diamond/cubic boron nitride interfaces, 2025, ArXiv Preprint.

[44] A.J. Gabourie, Z. Fan, T. Ala-Nissila, E. Pop, Spectral decomposition of thermal conductivity: Comparing velocity decomposition methods in homogeneous molecular dynamics simulations, Phys. Rev. B 103 (20) (2021) 205421, http://dx.doi.org/10.1103/PhysRevB.103.205421.

[45] S. Li, Z. Tong, X. Zhang, H. Bao, Thermal conductivity and lorenz ratio of metals at intermediate temperatures with mode-level first-principles analysis, Phys. Rev. B 102 (17) (2020) 174306, http://dx.doi.org/10.1103/PhysRevB.102.174306.

[46] J.R. Olson, R.O. Pohl, J.W. Vandersande, A. Zoltan, T.R. Anthony, W.F. Banholzer, Thermal conductivity of diamond between 170 and 1200 K and the isotope effect, Phys. Rev. B 47 (22) (1993) 14850–14856, http://dx.doi.org/10.1103/PhysRevB.47.14850.

[47] D.G. Onn, A. Witek, Y.Z. Qiu, T.R. Anthony, W.F. Banholzer, Some aspects of the thermal conductivity of isotopically enriched diamond single crystals, Phys. Rev. Lett. 68 (18) (1992) 2806–2809, http://dx.doi.org/10.1103/PhysRevLett.68.2806.

[48] Y. Ouyang, C. Yu, J. He, P. Jiang, W. Ren, J. Chen, Accurate description of high-order phonon anharmonicity and lattice thermal conductivity from molecular dynamics simulations with machine learning potential, Phys. Rev. B 105 (11) (2022) 115202, http://dx.doi.org/10.1103/PhysRevB.105.115202.

[49] F. Tian, B. Song, X. Chen, N.K. Ravichandran, Y. Lv, K. Chen, S. Sullivan, J. Kim, Y. Zhou, T.-H. Liu, M. Goni, Z. Ding, J. Sun, G.A.G. Udalamatta Gamage, H. Sun, H. Ziyaee, S. Huyan, L. Deng, J. Zhou, A.J. Schmidt, S. Chen, C.-W. Chu, P.Y. Huang, D. Broido, L. Shi, G. Chen, Z. Ren, Unusual high thermal conductivity in boron arsenide bulk crystals, Science 361 (6402) (2018) 582–585, http://dx.doi.org/10.1126/science.aat7932.

[50] Z. Tong, S. Li, X. Ruan, H. Bao, Comprehensive first-principles analysis of phonon thermal conductivity and electron-phonon coupling in different metals, Phys. Rev. B 100 (14) (2019) 144306, http://dx.doi.org/10.1103/PhysRevB.100.144306.

[51] Y. Wang, Z. Lu, X. Ruan, First principles calculation of lattice thermal conductivity of metals considering phonon-phonon and phonon-electron scattering, J. Appl. Phys. 119 (22) (2016) 225109, http://dx.doi.org/10.1063/1.4953366.

[52] H. Cao, Z. Tan, M.-H. Lu, G. Ji, X.-J. Yan, C. Di, M. Yuan, Q. Guo, Y. Su, A. Addad, Z. Li, D.-B. Xiong, Graphene interlayer for enhanced interface thermal conductance in metal matrix composites: An approach beyond surface metallization and matrix alloying, Carbon 150 (2019) 60–68, http://dx.doi.org/10.1016/j.carbon.2019.05.004.

[53] L. Chen, S. Chen, Y. Hou, Understanding the thermal conductivity of diamond/copper composites by first-principles calculations, Carbon 148 (2019) 249–257, http://dx.doi.org/10.1016/j.carbon.2019.03.051.

[54] C. Monachon, L. Weber, Thermal boundary conductance of transition metals on diamond, Emerg. Mater. Res. 1 (2) (2012) 89–98, http://dx.doi.org/10.1680/emr.11.00011.

[55] Y. Wu, J. Luo, Y. Wang, G. Wang, H. Wang, Z. Yang, G. Ding, Critical effect and enhanced thermal conductivity of cu-diamond composites reinforced with various diamond prepared by composite electroplating, Ceram. Int. 45 (10) (2019) 13225–13234, http://dx.doi.org/10.1016/j.ceramint.2019.04.008.

[56] B. Xu, S.-W. Hung, S. Hu, C. Shao, R. Guo, J. Choi, T. Kodama, F.-R. Chen, J. Shiomi, Scalable monolayer-functionalized nanointerface for thermal conductivity enhancement in copper/diamond composite, Carbon 175 (2021) 299–306, http://dx.doi.org/10.1016/j.carbon.2021.01.018.

[57] B. Liu, M. Wang, Interfacial thermal transport driven by phonon wave behaviors and its tunability in GaN-on-diamond devices, Int. J. Heat Mass Transfer 229 (2024) 125700, http://dx.doi.org/10.1016/j.ijheatmasstransfer.2024.125700.

[58] J. Xu, Y. Guo, Uncovering the roughness effect on inelastic phonon scattering and thermal conductance at interface via spectral energy exchange, Int. J. Heat Mass Transfer 250 (2025) 127295, http://dx.doi.org/10.1016/j.ijheatmasstransfer.2025.127295.

[59] S. Hu, M. An, N. Yang, B. Li, Manipulating the temperature dependence of the thermal conductivity of graphene phononic crystal, Nanotechnology 27 (26) (2016) 265702, http://dx.doi.org/10.1088/0957-4484/27/26/265702.

[60] L. Yang, J. Chen, N. Yang, B. Li, Significant reduction of graphene thermal conductivity by phononic crystal structure, Int. J. Heat Mass Transfer 91 (2015) 428–432, http://dx.doi.org/10.1016/j.ijheatmasstransfer.2015.07.111.
[61] L. Yang, N. Yang, B. Li, Extreme low thermal conductivity in nanoscale 3D si phononic crystal with spherical pores, Nano Lett. 14 (4) (2014) 1734–1738, http://dx.doi.org/10.1021/nl403750s.
[62] X. Wan, D. Pan, Z. Zong, Y. Qin, J.-T. Lü, S. Volz, L. Zhang, N. Yang, Modulating thermal conductivity via targeted phonon excitation, Nano Lett. 24 (23) (2024) 6889–6896, http://dx.doi.org/10.1021/acs.nanolett.4c00478.
[63] Z. Zhang, Y. Guo, M. Bescond, J. Chen, M. Nomura, S. Volz, Generalized decay law for particlelike and wavelike thermal phonons, Phys. Rev. B 103 (18) (2021) 184307, http://dx.doi.org/10.1103/PhysRevB.103.184307.
[64] Z. Zhang, Y. Guo, M. Bescond, J. Chen, M. Nomura, S. Volz, Heat conduction theory including phonon coherence, Phys. Rev. Lett. 128 (1) (2022) 015901, http://dx.doi.org/10.1103/PhysRevLett.128.015901.
[65] Z. Zhang, Y. Guo, M. Bescond, J. Chen, M. Nomura, S. Volz, How coherence is governing diffuson heat transfer in amorphous solids, Npj Comput. Mater. 8 (1) (2022) 96, http://dx.doi.org/10.1038/s41524-022-00776-w.
[66] Z. Zhang, Y. Guo, M. Bescond, M. Nomura, S. Volz, J. Chen, Assessing phonon coherence using spectroscopy, Phys. Rev. B 107 (15) (2023) 155426, http://dx.doi.org/10.1103/PhysRevB.107.155426.
[67] H. Wei, Y. Hu, H. Bao, X. Ruan, Quantifying the diverse wave effects in thermal transport of nanoporous graphene, Carbon 197 (2022) 18–26, http://dx.doi.org/10.1016/j.carbon.2022.06.011.
[68] Y. Hu, T. Feng, X. Gu, Z. Fan, X. Wang, M. Lundstrom, S.S. Shrestha, H. Bao, Unification of nonequilibrium molecular dynamics and the mode-resolved phonon Boltzmann equation for thermal transport simulations, Phys. Rev. B 101 (15) (2020) 155308, http://dx.doi.org/10.1103/PhysRevB.101.155308.
[69] G. Chen, Phonon wave heat conduction in thin films and superlattices, J. Heat Transf. 121 (4) (1999) 945–953, http://dx.doi.org/10.1115/1.2826085.
[70] B. Liu, Y. Guo, V.I. Khvesyuk, A.A. Barinov, M. Wang, Heat conduction of multilayer nanostructures with consideration of coherent and incoherent phonon transport, Nano Res. 15 (10) (2022) 9492–9497, http://dx.doi.org/10.1007/s12274-022-4589-7.
[71] S. Tamura, D.C. Hurley, J.P. Wolfe, Acoustic-phonon propagation in superlattices, Phys. Rev. B 38 (2) (1988) 1427–1449, http://dx.doi.org/10.1103/PhysRevB.38.1427.
[72] J. Achenbach, Wave Propagation in Elastic Solids, North-Holland Publishing Company, Amsterdam, 1973.
[73] B. Auld, Acoustic Fields and Waves in Solids, Wiley, New York, 1973.
[74] M. Maldovan, Phonon wave interference and thermal bandgap materials, Nat. Mater. 14 (7) (2015) 667–674, http://dx.doi.org/10.1038/nmat4308.